

HR-GLDD: A globally distributed dataset using generalized DL for rapid landslide mapping on HR satellite imagery

Sansar Raj Meena ¹, Lorenzo Nava ¹, Kushanav Bhuyan ¹, Silvia Puliero ¹, Lucas Pedrosa Soares ², Helen Cristina Dias ², Mario Floris ¹, Filippo Catani ^{1*}

1. Machine Intelligence and Slope Stability Laboratory, Department of Geosciences, University of Padova, 35129 Padua, Italy
2. Institute of Energy and Environment, University of São Paulo, São Paulo 05508-010, Brazil

* Correspondence: sansarraaj.meena@unipd.it

Abstract:

Multiple landslide events occur often across the world which have the potential to cause significant harm to both human life and property. Although a substantial amount of research has been conducted to address mapping of landslides using Earth Observation (EO) data, several gaps and uncertainties remain when developing models to be operational at the global scale. The lack of a high resolution globally distributed and event-diverse dataset for landslide segmentation poses a challenge in developing machine learning models that can accurately and robustly detect landslides in various regions, as the limited representation of landslide and background classes can result in poor generalization performance of the models. To address this issue, we present the high-resolution global landslide detector database (HR-GLDD), a high resolution (HR) dataset for landslide mapping composed of landslide instances from ten different physiographical regions globally: South and South-East Asia, East Asia, South America, and Central America. The dataset contains five rainfall triggered and five earthquake-triggered multiple landslide events that occurred in varying geomorphological and topographical regions. HR-GLDD is one of the first dataset for landslide detection generated by high resolution satellite imagery which can be useful for applications in artificial intelligence for landslide segmentation and detection studies. Five state of the art deep learning models were used to test the transferability and robustness of the HR-GLDD. Moreover, two recent landslide events were used for testing the performance and usability of the dataset to comment on the detection of newly occurring significant landslide events. The deep learning models showed similar results for testing the HR-GLDD in individual test sites thereby indicating the robustness of the dataset for such purposes. The HR-GLDD can be accessed open access and it has the potential to calibrate and develop models to produce reliable inventories using high resolution satellite imagery after the occurrence of new significant landslide events. The HR-GLDD will be updated regularly by integrating data from new landslide events.

1. Introduction

With the increasing impacts of climate change, increased urbanization, and anthropogenic pressure in recent years, the risk from hazards to population, infrastructure, and essential life services has exacerbated. Landslides are quite ubiquitous and account for approximately 4.9% of all the natural disasters and 1.3% of the fatalities in the world (EM-DAT, 2018). Induced by natural (earthquakes, volcanic eruptions, meteorological events) and anthropogenic triggers (slope modifications, mining, landscape engineering), the increase in the stress of slope materials causes landslides, which can harm numerous elements at risk. Landslides occur heterogeneously in many parts of the world including the Central and South Americas, the Caribbean islands, Asia, Turkey, European Alps, and East Africa (Froude & Petley, 2018). In the past 15 years, we have seen a high number of events that have

50 inadvertently led to the failure of thousands of slopes and causing damage to essential linear
51 infrastructures and population. Some recent examples are Wenchuan, China (2008),
52 Kedarnath, India (2013), Kaikoura, New Zealand (2016), Jiuzhaigou, China (2017), Dominica
53 (2017), Porgera, Papua New Guinea (2018), Hokkaido, Japan (2018), Belluno, Italy (2018),
54 Haiti (2021), Sumatra, Indonesia (2022).

55 These examples indicate that landslide occurrences will probably continue to increase in the
56 short and medium term; therefore, an effective capability of rapid mapping is required to map
57 future event-based landslides. In recent years, state-of-the-art research has been conducted
58 to better understand the impact of natural hazards such as landslides and the cascading
59 effects on the elements-at-risk. A critical understanding of these complex processes begins
60 with the onset of mapping slope failures. This information about the failed slopes is attributed
61 as records and is documented in a “landslide inventory”. Landslide inventories include
62 information on the spatial location and extent of the landslides and, if available, also crucial
63 information about 1) the time of occurrence, 2) the triggering event that led slopes to fail, 3)
64 the typology of the landslides based on the accepted standard classifications like (Cruden &
65 Varnes, 1996) and (Hung et al., 2014), and 4) the volume of the failure. However, regarding
66 rapid mapping of recently occurred landslides, information about the spatial location,
67 distribution, and intersection with affected elements-at-risk are important. , and 4) the volume
68 of the failure. However, regarding rapid mapping of recently occurred landslides, information
69 about the spatial location, distribution, and intersection with affected elements-at-risk are
70 important.

71 When it comes to detecting and mapping landslides over remotely sensed images, it is safe
72 to say that a lot of the current literature in the past couple of years has devised and spent time
73 employing artificial intelligence (AI) models to map landslides automatically, arguably, with
74 good results. These AI models can classify remote sensing images to denote where the
75 landslides are present in the analysed images. However, the core prerequisite for employing
76 AI models is a reliable dataset to be used for training. Recent studies have only focused on
77 mapping landslides with AI but at scales that are small or regional while also claiming that the
78 proposed models can cater towards rapid mapping of landslides at any given time, location
79 and scale (Liu et al., 2022; Meena et al., 2022a; Nava, Bhuyan, et al., 2022; Nava, Monserrat,
80 et al., 2022; Soares et al., 2022a; Tang et al., 2022; Yang et al., 2022; Yang & Xu, 2022).
81 However, seldom has been the case where truly an approach has been taken to map
82 landslides outside the regions where the models are initially trained on, and also towards
83 actually applying the proposed models in capturing and mapping event-based landslides that
84 has recently occurred. Some other works at collectively detecting and mapping landslides of
85 different countries have been attempted by (Prakash et al., 2021) and (Ghorbanzadeh et al.,
86 2022), which showcases the power of employing AI at mapping landslides. Recently, Bhuyan
87 et al. (2023) made some strides at mapping landslides at larger spatiotemporal scales to
88 provide multi-temporal inventories of some famous events but more experiments in to explore
89 other geographical contexts are required. The core of the mentioned studies also heavily relies
90 on the availability of quantity and quality data for training an AI model. The accessibility of
91 such data can 1) allow a model to identify landslides that were caused by different types of
92 triggers (logically leading to the detection of different types of landslides), 2) to map landslides
93 in different parts of the world that vary geomorphologically, and 3) the applicability of the model
94 at mapping newly occurring landslides triggered by events in recent times. The contemporary
95 works of the current literature brings about a critical discussion about the availability and
96 accessibility of comprehensive and adequate data to effectively train models to detect
97 landslides. Both (Prakash et al., 2021) and (Ghorbanzadeh et al., 2022) have used open-
98 source Sentinel-2 imageries for multi-site landslide detection however, considering the fact
99 that the spatial resolution is 10 metres, a lot of small landslides are missed out or not

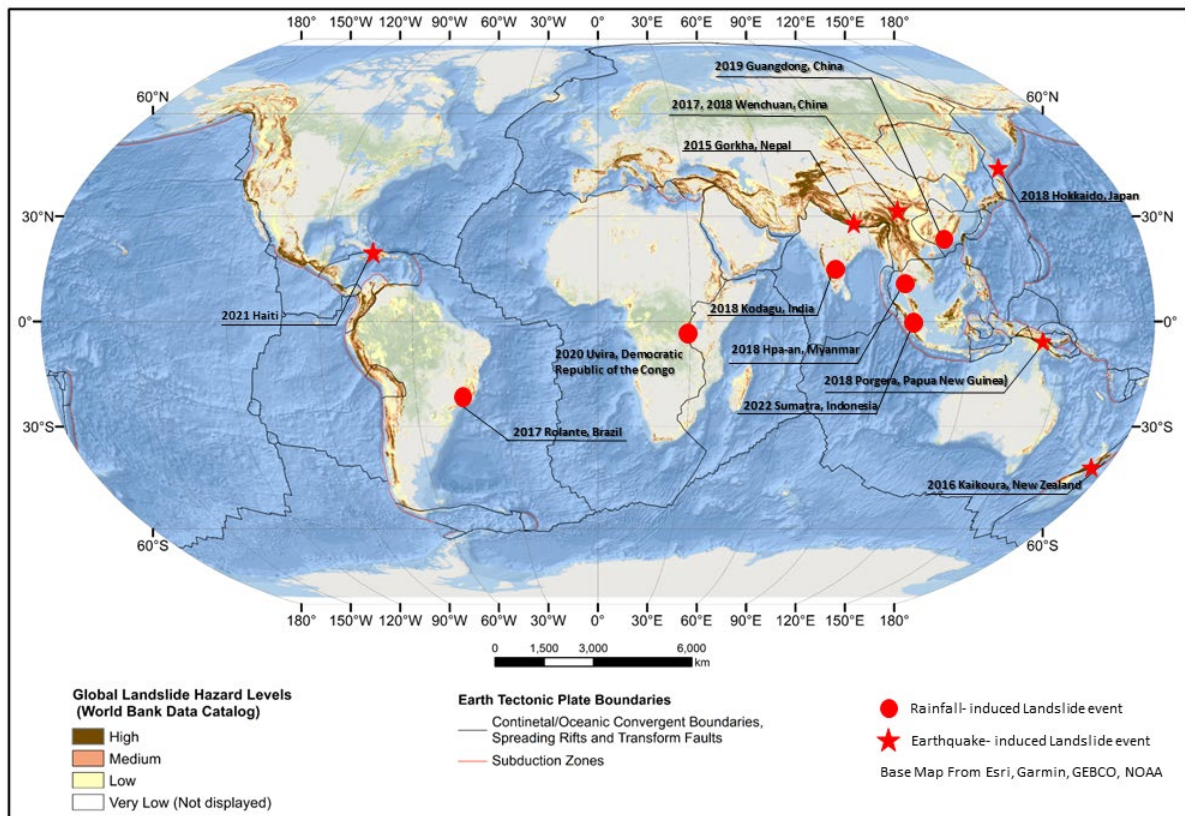
100 accurately captured (Meena et al., 2022b). The latter sampled data from 4 different
101 areas/events Sentinel-2 imagery (four bands at 10 meters spatial resolution, six at 20, and
102 three at 60) and combined it with DEM derived data from ALOS-PALSAR. The dataset we
103 propose, instead, is sampled from 10 different areas/events and uses 3 meters spatial
104 resolution imagery. Sampling from more areas can provide a more diverse representation of
105 both landslide and background classes, which can improve the robustness of the model when
106 applied to different regions. Moreover, a dataset with more diversity is likely to generalize
107 better to new unseen data than one with limited diversity, making it more suitable for real-
108 world deployment. Sampling from 10 areas also provides better coverage of the geographical
109 region, reducing the risk of missing important features or patterns. Higher spatial resolution
110 imagery captures more detail, allowing for more accurate identification and segmentation of
111 landslide features. It also allows obtaining a more detailed view, which can be useful to identify
112 small landslides or details that may be difficult to see in lower resolution imagery. Moreover, it
113 can provide more context for the location, helping to better understand the environment and
114 the relationships between different objects and features. Therefore, the increased detail can
115 result in improved accuracy when classifying features and objects, reducing the risk of
116 misclassification.

117 To effectively and rapidly map landslides after an event, it is required first to determine the
118 spatial extent of the affected areas. Collecting this data is frequently hazardous since it
119 involves individuals on the ground investigating landslides first hand during or immediately
120 after the event. With the increased availability of satellite imagery, this task has the potential
121 to be completed not only remotely but also automatically through the use of powerful deep
122 learning algorithms. Currently, adequate high-resolution satellite imagery of landslides is not
123 widely available. To depict the complex and dynamic nature of the landslides, significant
124 amounts of images must be provided. To this purpose, we present high-resolution global
125 landslide detector database (HR-GLDD), a large-scale satellite image dataset with assembled
126 landslide inventories. The database currently houses 10 geographical areas and 3 recently
127 transpired events (see Figure 1), and we plan to constantly update this database with newer
128 events.

129

130 2. Study areas

131 The study areas were chosen based on the variety of triggering events that resulted in the
132 occurrence of the landslides. Because of the availability of VHR archived Planet Scope
133 imageries after 2016, the most significant landslide events were considered. The
134 geomorphological diversity of the study sites results in a collection of complex landslide
135 phenomenon. We selected the imageries based on the availability of cloud-free conditions in
136 the areas and examined globally archived satellite remote sensing imageries from Planet
137 Scope from the years between 2017 and 2022 (Table 1). We selected 8 study sites across the
138 globe to assemble the database (see figure1). To further test the generalization capabilities of
139 the models trained on the proposed dataset, we choose three recently occurred events: co-
140 seismic landslides in Haiti (August, 2021) and rainfall-induced landslides in Indonesia
141 (February, 2022) and Democratic Republic of Congo (April, 2020).



142

143 Figure 1: Collection of rainfall- and earthquake-induced landslide events present in the HR-
 144 GLDD.

145

146 2.1. Papua New Guinea

147 Papua New Guinea (PNG) is located on the Australian continent and is the eastern half sector
 148 of the New Guinea island. The region is characterized by active volcanos, earthquakes,
 149 elevations up to ~4.400 m.a.s.l., steep slopes and is part of the 'Ring of Fire' in the Pacific
 150 Ocean. Regarding the tectonic and geological elements, the island can be divided into four
 151 tectonic belts: Stable platform, Fold Belt, Mobile Belt, and Papuan Fold and Thrust Belt
 152 (Tanyaş et al. 2022). The east sector, where PNG is located has the presence of accreted
 153 Paleozoic structure of Tasman Orogen (Hill and Hall, 2003). Due to these conditions, the area
 154 is frequently affected by landslides associated with the occurrence of earthquakes (Tanyaş et
 155 al. 2022). On February 25, 2018, in the southern area of the Papuan Fold and Thrust belt
 156 (central highlands of PNG), a severe earthquake occurred, the magnitude hit Mw 7.5. The
 157 event was responsible for damage to buildings, and energy structures besides triggering a
 158 high number of landslides (Wang et al. 2020). Around 11,600 landslide scars were registered,
 159 and more than half had 50,000 m² (Tanyaş et al. 2022), according to Wang et al. 2020, the
 160 earthquake hit the highest magnitude in the region in the past 100 years.

161 2.2. Kodagu, India

162 Kodagu district is located in the Karnataka state, Western Ghats, India. The area is
 163 characterized by elevations approximately between 50 and 1.750 m a.s.l., metamorphic
 164 rocks (e.g., amphibolite, gneiss, and schist), steep slopes, high annual precipitation of about
 165 4000 mm, and the presence of croplands (e.g., coffee, rice, and spices) (Jennifer and

166 Saravan, 2020; Meena et al. 2021). In August 2018, a rainfall-induced high magnitude mass
167 movement event occurred in Kodagu, the primary landslide type triggered was debris flow
168 (Meena et al. 2021). A total of 343 landslides were recorded, including mudflows, rock falls,
169 and debris flows (Meena et al. 2021). The event resulted in several damages to land
170 resources, properties, and loss of human lives (Martha et al. 2018; Jennifer and Saravan,
171 2020).

172 2.3. Rolante, Brazil

173 The Rolante river catchment study area is located in the Rio Grande do Sul state, southern
174 Brazil. The region being part of the Serra Geral geomorphological unit, has elevations up to
175 ~1.000 m.a.s.l. (Uehara et al. 2020). Moreover, is characterized by the presence of basaltic
176 rocks and sandstones, and annual precipitation thresholds between 1700 and 2000 mm
177 (Uehara et al. 2020, Soares et al. 2022). On 5 January 2017, a high magnitude rainfall-induced
178 mass movement event was triggered, and 308 landslides were registered (Gameiro et al.
179 2019; Quevedo et al. 2019), resulting in several damages to the Rolante municipality.

180 2.4. Tiburon Peninsula, Haiti

181 The Tiburon Peninsula study area is located in the western part of the Hispaniola island (Haiti)
182 with elevation up to 2300 m. a.s.l. Tiburon Peninsula, mainly consists of volcanic rocks such
183 as basalts and sedimentary rocks, namely limestones (Harp et al., 2016). The annual
184 precipitation of the area is more than 1600 mm (Alpert, 1942; USAID, 2014). On 14 August
185 2021, Tiburon Peninsula was struck by a Mw 7.2 earthquake, which was followed by several
186 aftershocks. The strongest one (Mw 5.7) occurred on 15 August 2021. Two days after the
187 mainshock the area was hit by the intense Tropical Cyclone Grace. The combination of the
188 two events triggered thousands of landslides (Martinez et al., 2021) in the Pic Macaya National
189 Park located in western part of the peninsula.

190 2.5. Rasuwa, Nepal

191 The study area is located in the Rasuwa district (central Nepal) in the higher Himalayas with
192 altitudes ranging from 904 to 3267 m. a.s.l and annual average precipitation of 1800-2000 mm
193 (Karki et al., 2016), The geology includes Proterozoic metamorphic rocks such as amphibolite,
194 gneiss, and schist (Tiwari et al., 2017). The area was struck by the Mw 7.8 Gorkha earthquake
195 on 25 April 2015. The intense seismic sequence produced at least 25,000 landslides (Roback
196 et al., 2018).

197 2.6. Hokkaido, Japan

198 The Hokkaido study area is in northern Japan and has a high presence of croplands. The area
199 is characterized by elevations between 50 and 500 m a.s.l., the geology is composed of
200 Neogene sedimentary rocks, formed by the accumulation of numerous layers formed by
201 materials ejected by the Tarumai volcano from several events over the years (Yamagishi and
202 Yamazaki, 2018; Zhao et al. 2020; Koi et al. 2022). A severe earthquake hit the Hokkaido
203 Iburi-Tobu area in Japan on September 6th, 2018. The earthquake registered a magnitude of
204 6.7 according to the Japan Meteorological Agency (JMA) and its epicenter was at 42.72° North
205 and 142.0° East (Yamagishi and Yamazaki, 2018), located along the southern frontier of
206 Hokkaido. The event triggered thousands of landslides (~7059) in a concentrated area of 466
207 km² (Zhao et al. 2020) and was responsible for 36 deaths (Yamagishi and Yamazaki, 2018).

208 2.7. Wenchuan, China

209 The study area is in the Longmenshan region at the eastern margin of the Tibetan Plateau,
210 China. The location is characterized by high elevations up to 7.500 m a.s.l., the geology

211 consists of lithological units from the Mesozoic, Jurassic, Cretaceous, Paleozoic, Precambrian
212 formations and three types of Quaternary sedimentary units (Qi et al. 2010; Gorum et al.
213 2011). The area is constantly affected by earthquake-induced landslides over the years (e.g.,
214 2017, 2018, 2019, 2021). The 2008 Wenchuan event is one of the most destructive events of
215 mass movements related to earthquakes in the region (Fan et al. 2018). The Wenchuan
216 earthquake hit a magnitude of Mw 7.9. It was responsible for triggering nearly 200.000
217 landslides (Xu et al. 2014), besides missing, injured, and thousands of human fatalities in a
218 total area of 31,686.12 km² (Qi et al. 2010).

219 2.8. Sumatra, Indonesia

220 The investigated area is Mount Talamau (2912 m) which is a compound volcano located in
221 West Pasaman Regency, West Sumatra Province, Indonesia. Geologically, the volcano
222 consists of andesite and basalt rocks belonging to Pleistocene-Holocene age (Fadhilah &
223 Prabowo, 2020; Zulkarnain, 2016). The climate of the area is humid and tropical and the mean
224 annual precipitation in West Pasaman area is between 3500 and 4500 mm/year (Wilis, 2019).
225 The Mw 6.1 earthquake hit West Sumatra on 25 February 2022. This event triggered several
226 landslides in an area of 6 km², along the eastern and north-eastern flank of Talamau volcano.

227 2.9. Longchuan, China

228 The study area is located in the vicinity of Mibei village in Longchuan County, Guangdong
229 Province, China with elevations between 180 and 600 m. The area has a subtropical monsoon
230 climate, affected by frequent typhoons and rainstorms from May to October. The average
231 annual precipitation ranges from 1300 to 2500 mm (Bai et al., 2021). The area is composed
232 of Paleozoic completely weathered granite and Quaternary granite residual soil (Bai et al.,
233 2021). Between 10 and 13 June 2019, an intense rainfall event, which was characterized by
234 cumulative rainfall of 270 mm, triggered 327 shallow landslides between 300 and 400 m of
235 altitudes and slopes ranging from 35 to 45° (Feng et al., 2022).

236 2.10. Hpa-An, Myanmar

237 The study area is located in Hpa-An district (central Kayin State, South Myanmar) in a tropical
238 and monsoon area with a mean annual precipitation between 4500 and 5000 mm (Win Zin &
239 Rutten, 2017) and elevations up to 1300 meters. The area is part of the Shan Plateau
240 sequence, which includes low grade metamorphosed Precambrian, Paleozoic and Mesozoic
241 sedimentary rocks (Jain & Banerjee, 2020). On 28–30 July 2018, Myanmar was hit by an
242 extreme rainfall event which caused a flood along Bago river basin and triggered 992
243 landslides only in Kayin State (Amatya et al., 2022).

244 2.11. Porgera, Papua New Guinea

245 The 2018 Papua New Guinea earthquake triggered over 200 landslides across the affected
246 region, resulting in fatalities and severe infrastructure damage. The landslides were primarily
247 caused by strong ground shaking and the steep topography of the region. Factors such as soil
248 characteristics, rainfall, and vegetation cover also played a role. Understanding these factors
249 can improve landslide hazard assessments and reduce future risk. Characteristics of the
250 landslides included high relief, steep slopes, and weak lithology. Effective strategies for
251 managing landslide hazards in high-risk areas should be developed. (Dang et al., 2020; Xu et
252 al., 2020).

253 2.12. Kaikoura, New Zealand

254 The 2016 Kaikoura earthquake triggered more than 10,000 landslides in New Zealand,
255 causing extensive damage and disrupting transportation routes. The landslides were complex

256 and involved multiple failure mechanisms, including rockfalls, rock avalanches, and debris
 257 flows. The intense shaking and steep topography of the region contributed to the landslides.
 258 To reduce the potential impact of future earthquakes, it is crucial to improve understanding of
 259 landslide mechanisms and develop effective early warning systems (Goda et al., 2020;
 260 Massey et al., 2020; Wang et al., 2020).

261 2.13. Uvira, Democratic Republic of Congo

262 The city of Uvira in the Democratic Republic of Congo experienced devastating landslides in
 263 2020 due to heavy rainfall, poor land management practices, and the steep topography of the
 264 region. These landslides caused significant damage to infrastructure and displaced thousands
 265 of people. Landslides are a recurring hazard in the DRC, with an average of 100 occurring
 266 annually, and climate change is expected to exacerbate the problem. Efforts to mitigate the
 267 risk of landslides can include improved land use practices, early warning systems, and
 268 infrastructure designed to withstand landslides. Taking a comprehensive approach is key to
 269 minimizing the impact of landslides and protecting at-risk communities. (Mwene-Mbeja et al.,
 270 2020; Kervyn et al., 2020; United Nations Office for Disaster Risk Reduction, 2020)

271 3. High-Resolution Global landslide Detector Database (HR-GLDD)

272

273 3.1. Data set description:

274 The dataset created in this study consists of images acquired from the PlanetScope satellites
 275 (see table 1) and landslide inventories collected from the literature. For all the events,
 276 landslides were manually delineated due to unavailability of existing inventories at high
 277 resolution. PlanetScope is a constellation of approximately 130 satellites that acquire images
 278 of the Earth daily with 3 meters of spatial resolution. The sensors acquire the images with 8
 279 spectral bands: coastal blue (431 - 552 nm), blue (465 - 515 nm), green (547 - 583 nm), yellow
 280 (600 - 620 nm), red (650 - 680 nm), red-edge (697 - 713 nm) and NIR (845 - 885 nm) (Planet
 281 Team, 2019). PlanetScope imagery consists of surface reflectance values and 16 bits images.
 282 The images from both sensors are orthorectified and radiometrically corrected by the
 283 providers.

284 The dataset was prepared using only the red, green, blue, and NIR bands. The pre-processing
 285 phase was based on three steps: generation of binary masks, data sampling, and tiles
 286 patching. First, the interpreted landslides polygons from each area were rasterized using the
 287 Rasterio Python library into a binary mask, where "1" represents the landslides and "0" the
 288 background. The satellite imagery, along with the mask was then sampled and patched into a
 289 regular grid that yields patches of dimension 128 x 128 pixels, which correspond to 14.7 km²
 290 per patch. Since the imbalance between background area and landslides is strong, the images
 291 that did not have any landslides pixel labelled were removed. The proportions for the positive
 292 samples of landslides against the non-landslides are 9.96% and 90.04%, respectively. Table
 293 1 shows the number of tiles created for each area.

294

295 Table 1 - Number of tiles, satellite information and landslide statistics for each study area.

Study Area	Satellite	Number of tiles	Study Area in km ²	Number of landslides	Minimum Landslide area (m ²)	Maximum Landslide area (m ²)	Total Landslide area (km ²)
------------	-----------	-----------------	-------------------------------	----------------------	--	--	---

Kodagu (India) 2018	PlanetScope	530	4033.62	343	276.23	581342.19	5.67
Rolante (Brazil) 2017	PlanetScope	33	24.62	113	381.76	81277.53	0.67
Tiburón Peninsula, (Haiti) 2021	PlanetScope	461	130.85	1394	200.74	473696	8.24
Rasuwa (Nepal) 2017	PlanetScope	222	114.68	184	676.85	115567.96	2.45
Hokkaido (Japan) 2018	PlanetScope	159	50.17	715	237.76	48524.72	5.29
Wenchuan (China) 2017	PlanetScope	284	58.25	1415	23.78	98467.96	3.19
Wenchuan (China) 2018	PlanetScope	263	58.25	546	110.18	1289210.19	5.54
Sumatra, (Indonesia) 2022	PlanetScope	403	22.56	584	302.26	6206089.32	9.73
Longchuan, (China) 2019	PlanetScope	110	32.22	228	235.21	61163.17	0.73
Hpa-An, (Myanmar) 2018	PlanetScope	101	28.38	540	101.23	88044.20	0.97
Papua New Guinea	PlanetScope	725	304.94	491	262.65	259392.71	5.48
New Zealand	PlanetScope	287	150.75	246	676.67	165943.82	3.50
Democratic Republic of the Congo	PlanetScope	247	38.64	394	500.25	106094.52	1.61

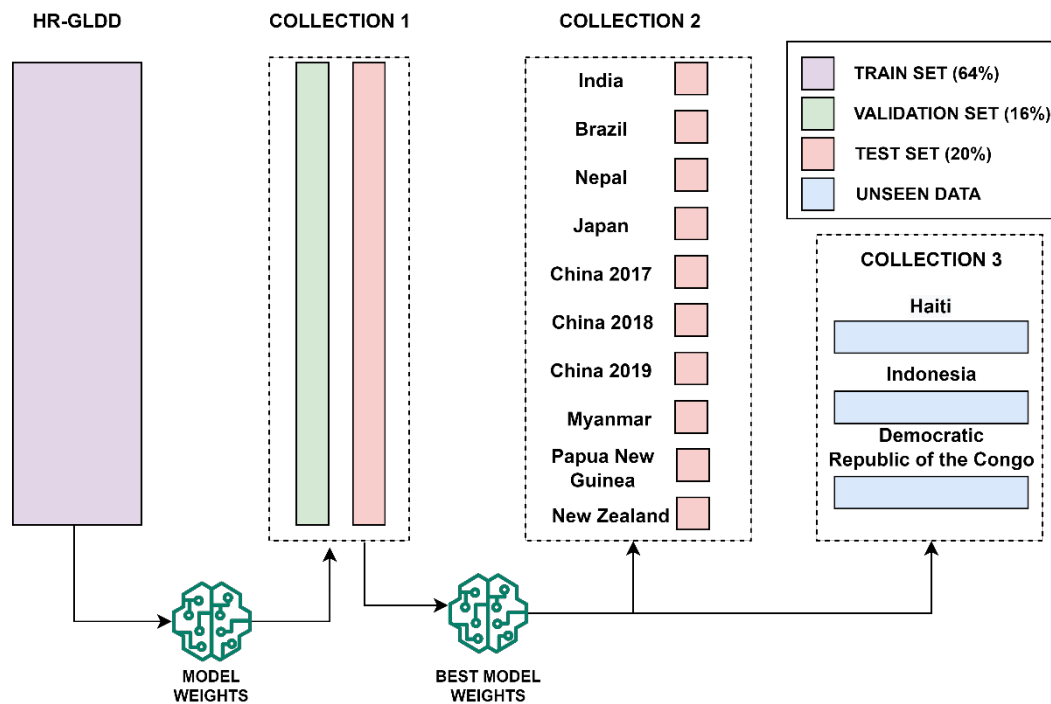
296

297 3.2. Design of HR-GLDD

298 The performance evaluation of the study sites was carried out using metrics and trained using
 299 five state-of-the-art U-Net like models, showcasing the capability and applicability of the High-
 300 Resolution Global Landslide Detector Database (HR-GLDD). We used a total of ten

301 geographically distinct study sites distributed globally, where landslide events were chosen
 302 including different triggering mechanisms such as five earthquake-induced and five rainfall-
 303 landslides-, we separately divide the patches into 60% for training, 20% for validation, and
 304 20% for testing the model capabilities. All the sets are then mixed to create a unique dataset
 305 composed of equal percentages of patches.

306 We designed three scenarios to train, predict, and evaluate model performances in order to
 307 assess the robustness and applicability of the HR-GLDD. Primarily, we evaluate the model
 308 performances on the individual test sets. Secondly, we evaluate the performances of the
 309 models on the HR-GLDD test set. Moreover, finally, we test on two completely unseen recently
 310 occurred landslide events in Haiti 2021 and Indonesia 2022 (see figure 2).



311

312 Figure 2: Schematic representation of the division of different components of HR-GLDD.
 313 Collection 1 refers to the test and validation data separated from the HR-GLDD. Collection 2
 314 refers to the test dataset of individual sites. Collection 3 refers to the data from three recent
 315 events for testing purposes.

316 4. Methodology

317

318 4.1. Model Architectures

319 The proposed dataset is evaluated through several state-of-the-art U-Net like Deep Learning
 320 segmentation models. In the past years, the U-Net (Abderrahim et al., 2020) has been used
 321 in several landslide detection applications which yield generally the most reliable results
 322 (Bhuyan et al., 2022; Meena et al., 2022c; Nava, Bhuyan, et al., 2022). Therefore, we decided
 323 to use it as a benchmark model when training on the proposed dataset. Moreover, several
 324 improved versions of the same are evaluated. We systematically trained the model using a
 325 variety of combinations of the hyper-parameters batch size (8, 16, 32, 64), learning rate (5e-
 326 4, 10e-4, 5e-5, 10e-5) and the number of filters of the first convolutional layer (8, 16, 32, 64).
 327 A description of the employed architectures is given in this section.

328 U-Net: This architecture has been utilized in various semantic segmentation applications,
329 yielding generally outstanding results (Abderrahim et al., 2020). U-Net was employed initially
330 in biomedical picture segmentation (Ronneberger et al., 2015). Low-level representations are
331 captured by a contracting path (encoder), whereas a decoding path captures high-level
332 representations. The encoding path consists of successive convolution blocks and is
333 equivalent to a traditional CNN structure. Two convolutional layers with a 3 x 3 kernel size and
334 a 2 x 2 max-pooling layer are present within every convolutional block. The rectified linear unit
335 (ReLU) activation function is used to activate each convolutional layer (Agarap, 2018). A 2 x
336 2 max-pooling layer is added to the convolutional block's end in the encoder route to conduct
337 non-linear downsampling, whereas, in the decoder path, a 2 x 2 upsampling layer takes its
338 place. The upsampling layer is positioned right after a 3x3 convolutional layer (see figure S1).
339 We refer to this combination as learnable upconvolution. We refer to this combination as
340 learnable upconvolution.

341 Residual U-Net (Res U-Net): Res U-Net (Diakogiannis et al., 2020) follows the same U shape
342 as U-Net, whereas here the above-explained convolutional blocks are replaced by residual
343 blocks. This architecture's goal is to improve the learning capacities of the conventional U-Net
344 as well as mitigate the gradient vanishing effect, especially when dealing with deep neural
345 networks (such as U-Net) (see figure S2).

346 Attention U-Net and Attention Res U-Net: In the conventional U-Net as well as in the Res U-
347 Net, cascading convolutions have been shown to provide false alerts for tiny objects with high
348 form variability (Oktay et al., 2018). To select pertinent spatial information from low-level maps
349 and therefore alleviate the problem, soft attention gates (AGs) are added (see figure S3, S4).
350 The attention gates are built on skip connections, which actively inhibit activations in
351 unnecessary areas, lowering the number of duplicated features (Abraham & Mefraz Khan,
352 2018).

353 Attention Deep Supervision Multi-Scale (ADSMS) U-Net: This architecture adopts the
354 Attention U-Net structure, while, in addition, multi-scale image pyramid inputs are fed to the
355 model, and a deep supervision strategy is applied (Abraham & Mefraz Khan, 2018). In
356 practice, multi-scale inputs enable the model to gather that class data, which is more readily
357 available at various sizes. This holds true for both background features and landslides. Lastly,
358 where training data are few and networks are relatively shallow, deep supervision conducts a
359 potent "regularization". More details about the deep supervision strategy used are available in
360 the following section (see figure S5).

361

362 4.2. Model training

363

364 To train the DL models, we utilized Dice Loss (Milletari et al., 2016) as the loss function:

365

366 Dice Loss = $c \frac{1}{N_i} \frac{p_i c_i}{c_i + p_i}$

367

368 Equation (1) illustrates a two-class Dice score coefficient (DSC) variation for class c , where
369 $g_i c_i$ [0, 1] and $p_i c_i$ [0, 1] are the ground truth and predicted labels, respectively. Furthermore,
370 the numerical stability is assured by avoiding division by zero, while N specifies the total
371 number of picture pixels. As an exception, in the ADSMS U-Net model, every high-dimensional
372 feature representation is regulated by Focal Tversky Loss to avoid loss over-suppression,
373 while the final output is controlled by the conventional Tversky Loss. This deep supervision
374 strategy, described in Lee et al., (2015), requires intermediate layers to be semantically
375 discriminative at all scales. Furthermore, it contributes to ensuring that the attention unit has
376 the power to change responses to a wide variety of visual foreground material. This strategy
377 is adopted from (Abraham & Mefraz Khan, 2018), who propose it along with the ADSMS U-
378 Net architecture. As the loss function optimizer, for all the models, we used a stochastic

379 gradient descent strategy based on an adaptive estimate of first- and second-order moments
380 (Adam), which is useful in problems with uncertain data and sparse gradients (Kingma & Ba,
381 2015). The precision, recall, F1-score, and Intersection Over Union (IOU) score, the most
382 common accuracy evaluation measures for segmentation models, all of which have been
383 utilized in several landslide detection studies, were used to measure how well the applied DL
384 models performed in detecting landslides. The appropriate combinations of hyper-parameters
385 must be used while training such DL models in order to optimize the model and, therefore,
386 output the best results.

387

388 5. Results

389

390 5.1. HR-GLDD evaluation results

391 The robustness and applicability of the HR-GLDD was tested using the best model weight.
392 We train and calibrate the models using the HR-GLDD. The best weights for each model are
393 selected based on the model performances on the mixed test set of the HR-GLDD dataset.
394 After running the models on test dataset, batch size of 16 and Adam optimiser with learning
395 rate 5.00E-04 resulted in best model weight. To further evaluate the efficiency and
396 generalization capabilities of the models, we use the model on three unseen datasets to map
397 landslides in the two different geomorphological areas that were recently affected by multiple
398 landslide events. We chose the most recent events one occurred after Uvira, Democratic
399 Republic of Congo (DRC) heavy rainfall event of April 2020. Haiti earthquake in August 2021,
400 one in Sumatra, Indonesia after a heavy rainfall event of February 2022. A total of 247, 461
401 and 403 unseen image patches were evaluated for DRC, Haiti and Indonesia, respectively.

402 Experimental results for landslide detection by utilising the HR-GLDD are presented in Table
403 2. Overall, all the models performed consistently in collections 2 and 3. The F1-score
404 evaluation results for each test case of all the models demonstrate the applicability of the HR-
405 GLDD training dataset for landslide detection results. The average F1-score for HR-GLDD test
406 dataset (collection 1) across all the models was around 0.7045. Furthermore, the same was
407 observed in the individual test sites in collection 2. We also notice that the Precision and
408 Recall are well balanced ranging between 0.6346-0.7661 and 0.6672-0.8121, respectively,
409 indicating stable model predictions. In collection 3, the metrics reveal positive outcomes in
410 terms of mapping the landslides following the respective events, with an average F1-score of
411 0.5562 for DRC, 0.7947 for Haiti and 0.8603 for Indonesia. The recall values are higher than
412 precision values for all the models resulting in average F1-score of 0.7045 (see table 2).
413 Higher values of recall in all models means that the models were able to identify landslide
414 labelled pixels. However due to the use of only the optical bands, the spectral signatures of
415 other similar features (such as riverbeds and flat barren areas) were labelled as landslides
416 which result in false predictions, thereby, accounting for lower precision.

417 In figure 3 we chose a single image patch to showcase the predictions of the various models
418 with respect to the referenced ground truth. Despite the differences in the spectral fingerprints
419 of the satellite images for each study site and the events initiated by an earthquake or rainfall,
420 the models were still capable of recognizing landslide features (see figure 4, 5 and 6).
421 Particularly, we were able to map the recent events in DRC (2020), Haiti (2021) and Indonesia
422 (2022).

423

424

425

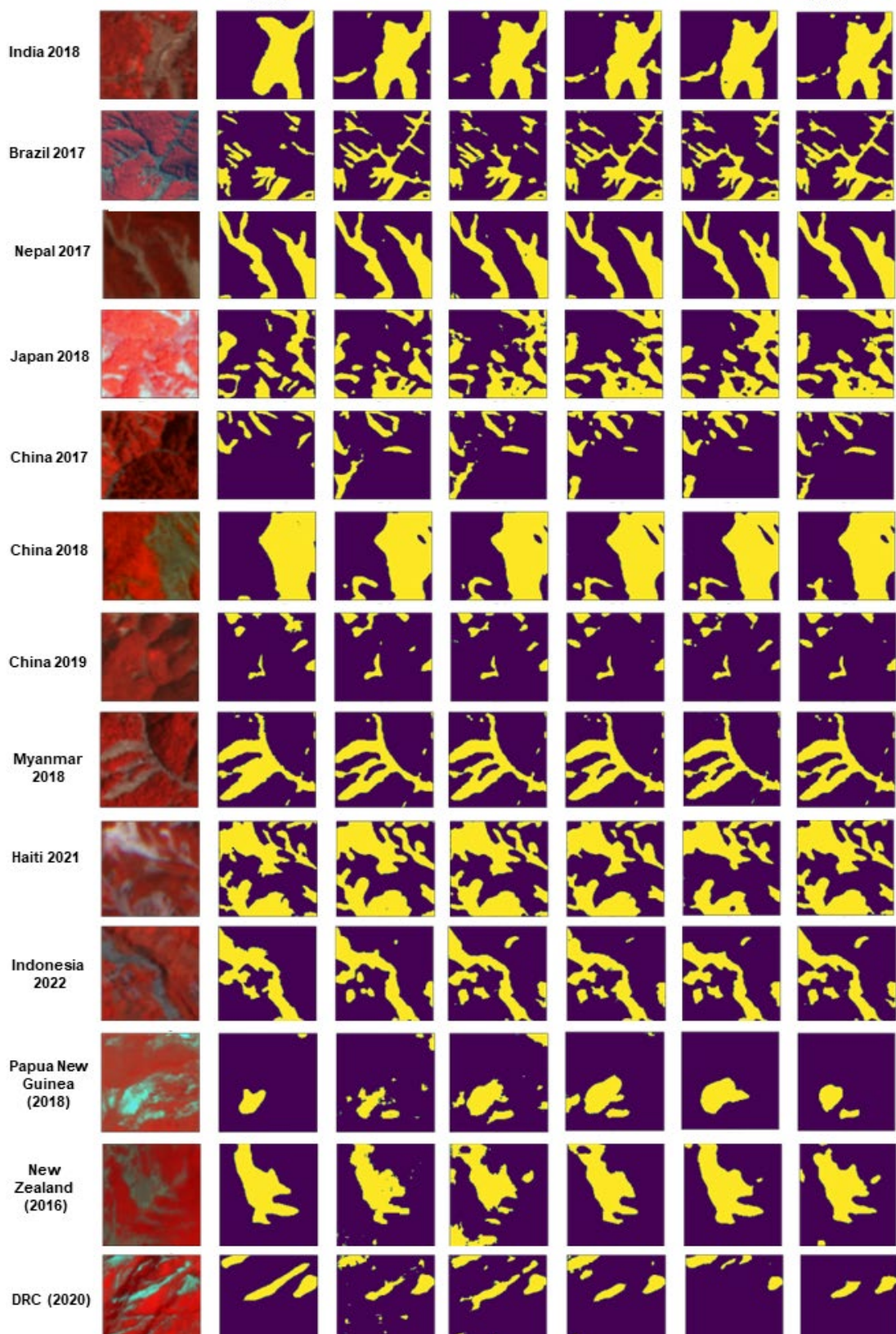
426
427

Table 2: F1 scores of different DL models across sites and HR-GLDD test dataset along with three unseen test sites.

<i>Study sites</i>		<i>U- NET</i>	<i>Res- U- NET</i>	<i>Attn- U- NET</i>	<i>Attn- res- Unet</i>	<i>ADSMS-U- NET</i>
Collection 1 (HR-GLDD Test)		0.7904	0.6825	0.7446	0.6477	0.6576
Collection 2	<i>India</i>	0.7674	0.6980	0.7628	0.6664	0.6796
	<i>Brazil</i>	0.7739	0.6913	0.6539	0.6830	0.6726
	<i>Nepal</i>	0.8972	0.8149	0.8419	0.7695	0.7976
	<i>Japan</i>	0.8159	0.7479	0.8124	0.7317	0.7552
	<i>Wenchuan (China2017)</i>	0.7781	0.6507	0.6981	0.6162	0.6739
	<i>Wenchuan (China2018)</i>	0.8077	0.6886	0.7295	0.6704	0.6557
	<i>Longchuan (China2019)</i>	0.6842	0.5076	0.5422	0.4829	0.4398
	<i>Myanmar</i>	0.8415	0.7861	0.7826	0.7405	0.7709
	<i>Papua New Guinea</i>	0.7515	0.6150	0.7568	0.6572	0.6261
	<i>New Zealand</i>	0.7496	0.5456	0.7335	0.4922	0.6494
Collection 3						
	<i>Indonesia</i>	0.8832	0.8810	0.8232	0.8534	0.8608
	<i>Haiti</i>	0.8357	0.8055	0.7869	0.7648	0.7808
	<i>Democratic Republic of the Congo</i>	0.5937	0.5366	0.5682	0.5008	0.5819

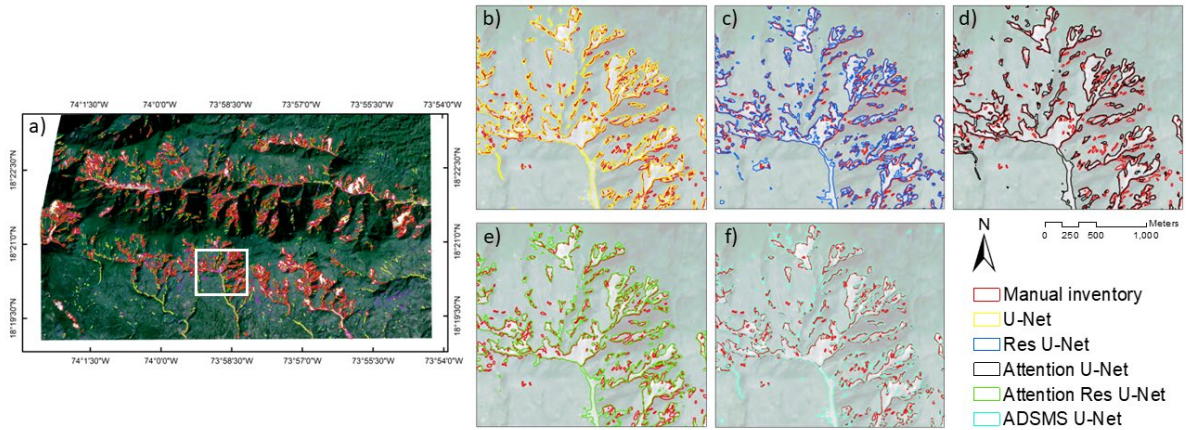
428

429



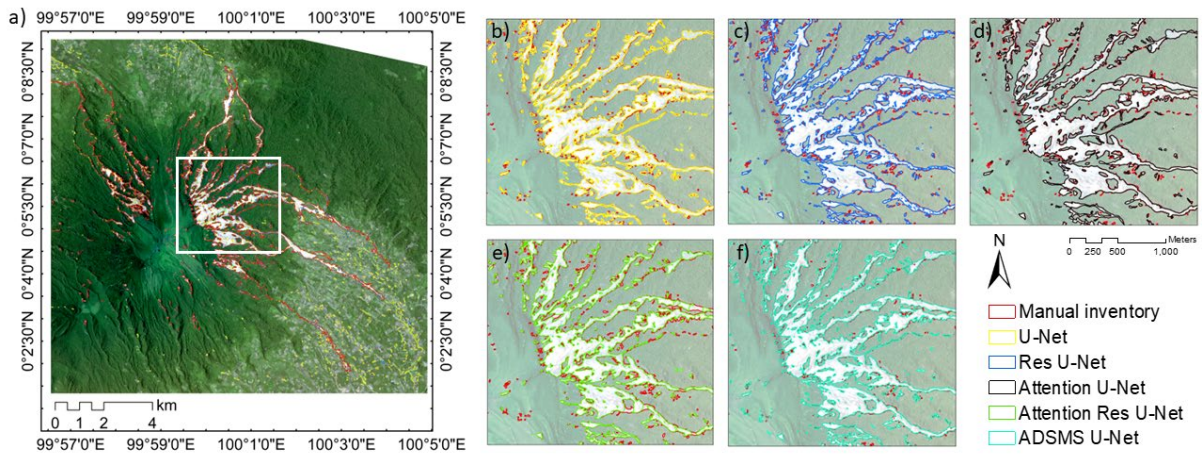
430

431 Figure 3: Landslide predictions made by the different DL models against the ground truth. The
 432 base image is shown as a false colour composite (FCC) to better visualize the scars of the
 433 landslides.



434

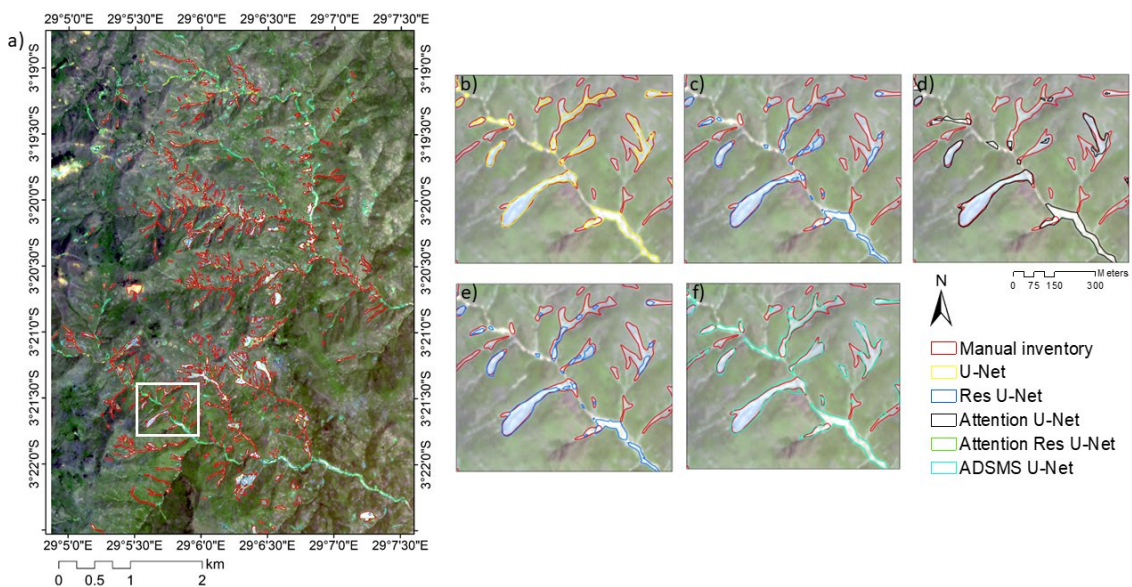
435 Figure 4: Comparison of ground truth landslides with predictions from the DL models for the
 436 unseen dataset of Haiti.



437

438 Figure 5: Comparison of ground truth landslides with predictions from the DL models for the
 439 unseen dataset of Indonesia.

440



441

442 Figure 6: Comparison of ground truth landslides with predictions from the DL models for the
443 unseen dataset of DRC.

444

445 6. Discussions

446 6.1. Advantages of using HR images

447 The spatial resolution of Planet Scope imagery enables the detection of small size landslides
448 that open access satellite missions like Sentinel and Landsat frequently miss due to their
449 spatial and temporal resolution (Meena et al., 2021). Moreover, even though Sentinel-2 has
450 additional spectral bands, the lack of improved spatial resolution inhibits precise boundary
451 delineation and landslide localisation (Meena et al., 2022). The most prominent features of
452 Planet Scope imagery, in addition to its competitive spatial resolution, are its daily temporal
453 resolution and global coverage. Since the satellites have identical sensors, the imageries
454 are orthorectified and image pre-processing are simplified and more accurate. Because
455 Planet imagery provide global coverage, we may extend our study sites to new locations for
456 generating more quality datasets that allow for a better model generalization.

457 6.2. Quality of HR-GLDD

458 The quality of any ML/DL model depends on the data that it is trained on, and the GLDD aims
459 to meet this fundamental requirement. To our knowledge, no other quality data sets exist that
460 can accommodate the wide range of landslide-triggering events and topographical diversity
461 needed for efficient model training. As the GLDD is a strong collection of various landslide
462 events caused both by rainfall and earthquakes. The GLDD is designed to calibrate models
463 able to map new events that will occur in the future. The models investigated in our study gave
464 promising and consistent results for two unseen datasets generated by completely different
465 events, indicating a well-prepared, dependable, and resilient dataset. However, there are clear
466 limitations with the GLDD that must be considered. These problems primarily stem from issues
467 with manually delineated polygons and various uncertainties caused by satellite imagery. A
468 number of different variables, including the mapping scale, the date, and the quality of the
469 satellite imagery, affect how accurate an inventory is. The radiometric resolution and cloud
470 coverage are additional variables that affect the generation of manual inventories. Additionally,
471 haze effect caused by instrument errors hinders model performances. Subjectivity in the
472 landslide polygon boundaries results from the amalgamation problem, which is caused by
473 elements like the investigators' level of experience and the goal of the study.

474 6.3. Significance of the HR-GLDD

475 A thorough hazard and risk framework is made possible by quality landslide inventories
476 however, the generating such inventories at large scales takes ample amount of time and
477 resources. This is where such automatic pipelines can truly shine at creating inventories which
478 can be used for the successive phases of a hazard and risk. Local, regional, and national
479 stakeholders may include such inventories into their risk reduction efforts thanks to the
480 availability of inventories produced automatically. Furthermore, this information may serve as
481 the foundation for a legal framework that implements landslide risk. A landslide risk reduction
482 plan is now more crucial than ever given the anticipated rise in worldwide landslide activity
483 brought on by climate change. Higher landslide activity is expected in the future due to a
484 number of factors, including an increase in the frequency and intensity of seismic events,
485 anthropogenic events, heavy precipitation events, rising ground water levels, storm surges,
486 and a general rise in relative sea level. Therefore, it is essential to comprehend the underlying
487 mechanisms of landslides better and create practical risk reduction techniques to save
488 people's lives and property.

489 6.4. Automated pipeline for HR-GLDD

490 At the moment, automated techniques are the only viable solution for mapping vast regions
491 with accuracy appropriate for operational objectives. Nonetheless, reliable, reproducible, and
492 accurate processes for automating landslide detection across huge data stacks are still
493 absent. As a result, many landslide-affected regions remain unmapped because 1) they are
494 challenging to map using standard methods, and 2) using high-resolution imagery is costly
495 and labour-intensive, with a substantial part of the mapping process dependent on human
496 judgment. By overcoming these challenges, automated pipelines that address these issues
497 can considerably reduce the requirement for human involvement and pave the way for the
498 development of reliable real-time mapping and monitoring of natural hazards at the continental
499 and global scales. Based on the quality of GLDD, reliability of automated pipelines and rapidly
500 growing availability of HR satellite imagery, we can realistically envision mapping of landslide
501 instances and contribute towards generating and updating landslide inventories at large-
502 scales, spatially and potentially, also temporally (Bhuyan et al., 2023).

503 Providing an expert-based, high-quality, and scientifically validated landslide inventory to
504 scientific communities is essential for frameworks of modelling, landslide prediction, machine
505 learning, and deep learning research. The GLDD dataset has been verified, which increases
506 the availability of much-needed training datasets for automated mapping algorithms. The
507 consistently long time taken to compile landslide inventories manually contrasts with the rise
508 in data accessible for landslide mapping. The development of technologies to successfully
509 automate the procedure is the future direction in landslide inventory mapping. The precedence
510 of quality dataset is noted in where they commented that the need for quality datasets will
511 provide a valuable resource for training and developing algorithms.

512 The current dataset is an excellent resource for training and developing future algorithms for
513 this purpose. Automated mapping methods, particularly when combined with publicly available
514 elevation models, can potentially improve our results in future investigations.

515 7. Conclusions

516 Mapping landslides through space is a challenging endeavour. Automated efforts for the same
517 have been explored to some extent, but a transferrable method based on a robust dataset has
518 not yet been investigated. In this paper, we propose a reliable dataset which can be employed
519 by deep learning algorithms to detect new landslides accurately. The predictive capabilities
520 demonstrate the usefulness and application of the dataset to map landslides at large scales.
521 However, the model's predictability must be investigated further in order to identify particular
522 problems to enhance the findings and predictive capabilities for more complicated landscapes.
523 Overall, despite the limitations, the findings are promising, since it is the first time such a HR
524 dataset has been created that caters to a transferable approach of mapping landslides at so
525 many different geomorphological and geographical locations.

526 Data availability

527 The data, working codes and a document with metadata are freely available at
528 [https://github.com/kushanavbhuyan/HR-GLDD-A-Global-Landslide-Mapping-Data-](https://github.com/kushanavbhuyan/HR-GLDD-A-Global-Landslide-Mapping-Data-Repository)
529 [Repository](https://github.com/kushanavbhuyan/HR-GLDD-A-Global-Landslide-Mapping-Data-Repository) where data in the format of arrays and model configurations in the framework of
530 TensorFlow as can be displayed and used for reproducibility of our results. We also submit
531 the generated landslide inventories in the form of an Environmental Systems Research
532 Institute (ESRI) shapefile. Modules for deep learning can be found at
533 <https://www.tensorflow.org/> and original satellite imageries can be found at
534 <https://www.planet.com/>.

535 Code availability

536 Code used to produce data described in this manuscript, as well as to create figures and
537 tables, can be accessed at [https://github.com/kushanavbhuyan/HR-GLDD-A-Global-](https://github.com/kushanavbhuyan/HR-GLDD-A-Global-Landslide-Mapping-Data-Repository)
538 [Landslide-Mapping-Data-Repository](https://github.com/kushanavbhuyan/HR-GLDD-A-Global-Landslide-Mapping-Data-Repository)

539 Author contribution

540 All the authors contributed to equally to preparation of manuscript from data curation to review
541 of final manuscript.

542 Competing interests

543 The authors declare that they have no conflict of interest.

544 **References**

545 Abderrahim, N. Y. Q., Abderrahim, S., & Rida, A. (2020). Road Segmentation using U-Net
546 architecture. 2020 IEEE International Conference of Moroccan Geomatics (Morgeo), 1–4.
547 <https://doi.org/10.1109/Morgeo49228.2020.9121887>

548 Abraham, N., & Mefraz Khan, N. (2018). A NOVEL FOCAL TVERSKY LOSS FUNCTION
549 WITH IMPROVED ATTENTION U-NET FOR LESION SEGMENTATION.
550 <https://github.com/nabsabraham/focal-tversky-unet>

551 Alpert, L. (1942). Rainfall map of Hispaniola. Bulletin of the American Meteorological Society,
552 23, 423–431.

553 Amatya, P., Kirschbaum, D., & Stanley, T. (2022). Rainfall-induced landslide inventories for
554 Lower Mekong based on Planet imagery and semi-automatic mapping method. Geoscience
555 Data Journal, 00, 1–13. <https://doi.org/10.1002/gdj3.145>

556 Bai, H., Feng, W., Yi, X., Fang, H., Wu, Y., Deng, P., Dai, H., & Hu, R. (2021). Group-occurring
557 landslides and debris flows caused by the continuous heavy rainfall in June 2019 in Mibe
558 Village, Longchuan County, Guangdong Province, China. Natural Hazards, 108(3), 3181–
559 3201. <https://doi.org/10.1007/s11069-021-04819-1>

560 Bhuyan, K., Tanyaş, H., Nava, L. *et al.* Generating multi-temporal landslide inventories through
561 a general deep transfer learning strategy using HR EO data. *Sci Rep* **13**, 162 (2023).
562 <https://doi.org/10.1038/s41598-022-27352-y>

563 Bhuyan, K., Meena, S. R., Nava, L., van Westen, C. J., Floris, M., & Catani, F. (2022). Mapping
564 landslides through a temporal lens: An insight towards multi-temporal landslide mapping using
565 the U-Net deep learning model. Earth Arxiv. <https://doi.org/https://doi.org/10.31223/X5DM0B>

566 Cruden, D. M., & Varnes, D. (1996). LANDSLIDE TYPES AND PROCESSES. In National
567 Research Council, Transportation Research Board.

568 Dang, K. T., Wang, G., Su, Y., Xu, Q., & Chen, W. (2020). Landslides triggered by the 2018
569 M7.5 earthquake in Papua New Guinea. Natural Hazards and Earth System Sciences, 20(6),
570 1647-1660.

571 Diakogiannis, F. I., Waldner, F., Caccetta, P., & Wu, C. (2020). ResUNet-a: A deep learning
572 framework for semantic segmentation of remotely sensed data. ISPRS Journal of
573 Photogrammetry and Remote Sensing, 162, 94–114.
574 <https://doi.org/10.1016/j.isprsjprs.2020.01.013>

575 EM-DAT. (2018). The emergency events database—Universit' e catholique de Louvain
576 (UCL)—CRED, D Guha-Sapir.

577 Fadhilah, & Prabowo, H. (2020). Genes and physical properties of iron sand from Kinali
578 Pasaman. *Journal of Physics: Conference Series*, 1481(1). <https://doi.org/10.1088/1742-6596/1481/1/012015>
579

580 Fan, X., Scaringi, G., Domènech, G., Yang, F., Guo, X., Dai, L., He, C., Xu, Q., & Huang, R.
581 (2019). Two multi-temporal datasets that track the enhanced landsliding after the 2008
582 Wenchuan earthquake. *Earth System Science Data*, 11(1), 35–55.
583 <https://doi.org/10.5194/essd-11-35-2019>

584 Feng, W., Bai, H., Lan, B., Wu, Y., Wu, Z., Yan, L., & Ma, X. (2022). Spatial-temporal
585 distribution and failure mechanism of group-occurring landslides in Mibei village, Longchuan
586 County, Guangdong, China. *Landslides*, May. <https://doi.org/10.1007/s10346-022-01904-9>

587 Fred Agarap, A. M. (n.d.). Deep Learning using Rectified Linear Units (ReLU). Retrieved
588 August 15, 2022, from <https://github.com/AFAgarap/relu-classifier>.

589 Froude, M. J., & Petley, D. N. (2018). Global fatal landslide occurrence from 2004 to 2016.
590 *Natural Hazards and Earth System Sciences*, 18(8), 2161–2181.
591 <https://doi.org/10.5194/nhess-18-2161-2018>

592 Ghorbanzadeh, O., Xu, Y., Ghamisi, P., Kopp, M., & Kreil, D. (2022). Landslide4Sense:
593 Reference Benchmark Data and Deep Learning Models for Landslide Detection.
594 <https://doi.org/10.48550/arxiv.2206.00515>

595 Goda, K., Ren, J., & Anderson, N. (2020). Landslides induced by the 2016 Kaikoura
596 earthquake, New Zealand: characteristics, distribution, and correlations. *Landslides*, 17(4),
597 825-839.

598 Harp, E. L., Jibson, R. W., & Schmitt, R. G. (2016). Map of landslides triggered by the January
599 12, 2010, Haiti earthquake. <https://doi.org/10.3133/sim3353>

600 Hungr, O., Leroueil, S., & Picarelli, L. (2014). The Varnes classification of landslide types, an
601 update. In *Landslides* (Vol. 11, Issue 2, pp. 167–194). Springer Verlag.
602 <https://doi.org/10.1007/s10346-013-0436-y>

603 Jain, A. K., & Banerjee, D. M. (2020). The Indian Subcontinent: Its tectonics. In *Proceedings*
604 *of the Indian National Science Academy* (Vol. 86, Issue 1).
605 <https://doi.org/10.16943/ptinsa/2020/49834>

606 Karki, R., Talchabhadel, R., Aalto, J., & Baidya, S. K. (2016). New climatic classification of
607 Nepal. *Theoretical and Applied Climatology*, 125(3–4), 799–808.
608 <https://doi.org/10.1007/s00704-015-1549-0>

609 Kervyn, M., Jacobs, L., Sumbwe, J., Maki Mateso, J. C., Kervyn, F., Sebagenzi, S. N., &
610 Havenith, H. B. (2020). Landslide hazard and risk assessment in the Democratic Republic of
611 Congo. *Landslides*, 17(8), 1901-1916.

612 Kingma, D. P., & Lei Ba, J. (n.d.). ADAM: A METHOD FOR STOCHASTIC OPTIMIZATION.

613 Lee, C.-Y., Xie, S., Gallagher, P., Zhang, Z., & Tu, Z. (n.d.). Deeply-Supervised Nets.

614 Liu, Y. ;, Yao, X. ;, Gu, Z. ;, Zhou, Z. ;, Liu, X. ;, Chen, X. ;, Wei, S., Liu, Y., Yao, X., Gu, Z.,
615 Zhou, Z., Liu, X., Chen, X., & Wei, S. (2022). Study of the Automatic Recognition of Landslides
616 by Using InSAR Images and the Improved Mask R-CNN Model in the Eastern Tibet Plateau.

617 Remote Sensing 2022, Vol. 14, Page 3362, 14(14), 3362.
618 <https://doi.org/10.3390/RS14143362>

619 Martinez, S. N., Allstadt, K. E., Slaughter, S. L., Schmitt, R. G., Collins, E., Schaefer, L. N., &
620 Ellison, S. (2021). Landslides triggered by the August 14, 2021, magnitude 7.2 Nippes, Haiti,
621 earthquake. Open-File Report.

622 Massey, C. I., Hancox, G. T., & Van Dissen, R. J. (2020). The 2016 Kaikoura, New Zealand,
623 Earthquake: A Complex Multihazard and Multirisk Event. *Annual Review of Earth and*
624 *Planetary Sciences*, 48, 235-259.

625 Meena, S. R., Ghorbanzadeh, O., van Westen, C. J., Nachappa, T. G., Blaschke, T., Singh,
626 R. P., & Sarkar, R. (2021). Rapid mapping of landslides in the Western Ghats (India) triggered
627 by 2018 extreme monsoon rainfall using a deep learning approach. *Landslides*, 18(5).
628 <https://doi.org/10.1007/s10346-020-01602-4>

629 Meena, S. R., Soares, L. P., Grohmann, C. H., van Westen, C., Bhuyan, K., Singh, R. P.,
630 Floris, M., & Catani, F. (2022). Landslide detection in the Himalayas using machine learning
631 algorithms and U-Net. *Landslides*, 19(5), 1209–1229. [https://doi.org/10.1007/s10346-022-](https://doi.org/10.1007/s10346-022-01861-3)
632 [01861-3](https://doi.org/10.1007/s10346-022-01861-3)

633 Milletari, F., Navab, N., and Ahmadi, S.-A. (2016). V-Net: Fully Convolutional Neural Networks
634 for Volumetric Medical Image Segmentation. In *Proceedings of the Fourth International*
635 *Conference on 3D Vision (3DV)*, 565-571. doi: 10.1109/3DV.2016.79.

636 Mwene-Mbeja, M., Mugaruka, J. P., Bisimwa, B., & Tchicaya, L. (2020). Landslide hazard and
637 risk assessment in Uvira city, Democratic Republic of Congo. *Environmental Hazards*, 19(3),
638 263-278.

639 Nava, L., Bhuyan, K., Meena, S. R., Monserrat, O., & Catani, F. (2022). Rapid Mapping of
640 Landslides on SAR Data by Attention U-Net. *Remote Sensing 2022*, Vol. 14, Page 1449,
641 14(6), 1449. <https://doi.org/10.3390/RS14061449>

642 Nava, L., Monserrat, O., & Catani, F. (2022). Improving Landslide Detection on SAR Data
643 Through Deep Learning. *IEEE Geoscience and Remote Sensing Letters*, 19.
644 <https://doi.org/10.1109/LGRS.2021.3127073>

645 Oktay, O., Schlemper, J., le Folgoc, L., Lee, M., Heinrich, M., Misawa, K., Mori, K., McDonagh,
646 S., Hammerla, N. Y., Kainz, B., Glocker, B., & Rueckert, D. (n.d.). Attention U-Net: Learning
647 Where to Look for the Pancreas.

648 Planet Team. (2019). Planet Imagery Product Specifications August 2019. 97.

649 Prakash, N., Manconi, A., & Loew, S. (2021). A new strategy to map landslides with a
650 generalized convolutional neural network. *Scientific Reports*, 11(1), 1–15.
651 <https://doi.org/10.1038/s41598-021-89015-8>

652 Roback, K., Clark, M. K., West, A. J., Zekkos, D., Li, G., Gallen, S. F., Chamlagain, D., & Godt,
653 J. W. (2018). The size, distribution, and mobility of landslides caused by the 2015 Mw7.8
654 Gorkha earthquake, Nepal. *Geomorphology*, 301, 121–138.
655 <https://doi.org/10.1016/j.geomorph.2017.01.030>

656 Ronneberger, O., Fischer, P., & Brox, T. (2015). U-Net: Convolutional Networks for Biomedical
657 Image Segmentation (pp. 234–241). https://doi.org/10.1007/978-3-319-24574-4_28

658 Soares, L. P., Dias, H. C., Garcia, G. P. B., & Grohmann, C. H. (2022a). Landslide
659 Segmentation with Deep Learning: Evaluating Model Generalization in Rainfall-Induced
660 Landslides in Brazil. *Remote Sensing*, 14(9), 2237. <https://doi.org/10.3390/rs14092237>

661 Tang, X., Tu, Z., Wang, Y., Liu, M., Li, D., & Fan, X. (2022). Automatic Detection of Coseismic
662 Landslides Using a New Transformer Method. *Remote Sensing*, 14(12), 2884.
663 <https://doi.org/10.3390/rs14122884>

664 Tiwari, B., Ajmera, B., & Dhital, S. (2017). Characteristics of moderate- to large-scale
665 landslides triggered by the Mw 7.8 2015 Gorkha earthquake and its aftershocks. *Landslides*,
666 14(4), 1297–1318. <https://doi.org/10.1007/s10346-016-0789-0>

667 United Nations Office for Disaster Risk Reduction. (2020). Landslide risk reduction in the Great
668 Lakes Region. Retrieved from [https://www.undrr.org/publication/landslide-risk-reduction-
669 great-lakes-region](https://www.undrr.org/publication/landslide-risk-reduction-great-lakes-region)

670 USAID. (2014). Haiti Securite Alimentaire en Bref.

671 Wang, F., Fan, X., Yunus, A. P., Siva Subramanian, S., Alonso-Rodriguez, A., Dai, L., Xu, Q.,
672 & Huang, R. (2019). Coseismic landslides triggered by the 2018 Hokkaido, Japan (Mw 6.6),
673 earthquake: spatial distribution, controlling factors, and possible failure mechanism.
674 *Landslides*, 16(8), 1551–1566. <https://doi.org/10.1007/s10346-019-01187-7>

675 Wang, T., Liu, C., Saito, H., Nishimura, Y., & Wang, G. (2020). Landslide susceptibility
676 mapping following the 2016 Kaikoura earthquake, New Zealand. *Landslides*, 17(11), 2617-
677 2630.

678 Wilis, R. (2019). Impact Variability of Rainfall Intensity to Horticulture Productivity at West
679 Pasaman Regency , Province of West Sumatera , Indonesia. *Core.Ac.Uk*, 7(10), 138–145.

680 Win Zin, W., & Rutten, M. (2017). Long-term Changes in Annual Precipitation and Monsoon
681 Seasonal Characteristics in Myanmar. *Hydrology: Current Research*, 08(02).
682 <https://doi.org/10.4172/2157-7587.1000271>

683 Xu, Q., Dang, K. T., Su, Y., Chen, W., & Wang, G. (2020). Characteristics of landslides
684 triggered by the 2018 M7.5 earthquake in Papua New Guinea. *Landslides*, 17(1), 145-157.

685 Yang, Z., & Xu, C. (2022). Efficient Detection of Earthquake-Triggered Landslides Based on
686 U-Net++: An Example of the 2018 Hokkaido Eastern Iburi (Japan) Mw = 6.6 Earthquake.
687 *Remote Sensing*, 14(12), 2826. <https://doi.org/10.3390/rs14122826>

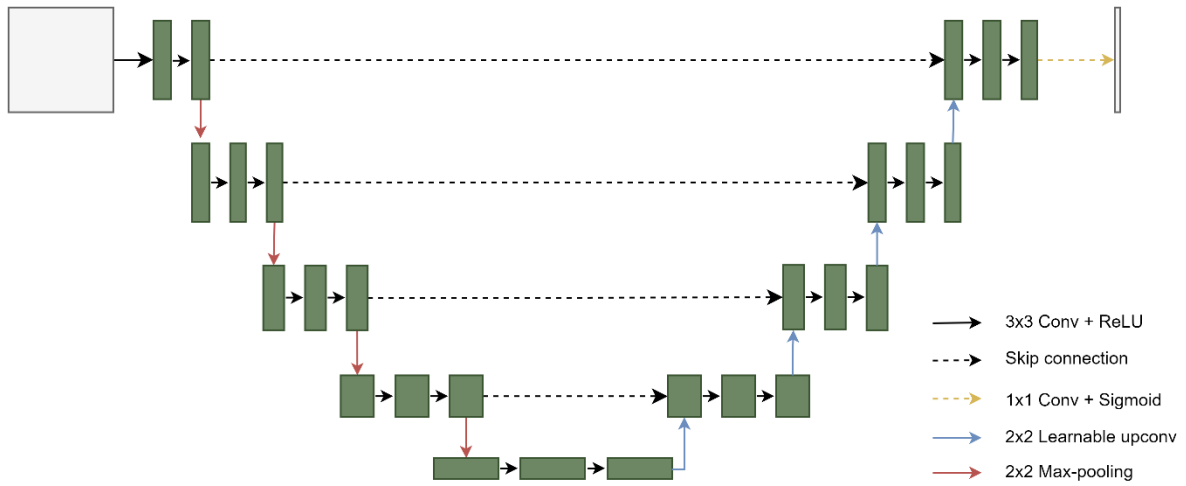
688 Yang, Z., Xu, C., & Li, L. (2022). Landslide Detection Based on ResU-Net with Transformer
689 and CBAM Embedded: Two Examples with Geologically Different Environments. *Remote
690 Sensing*, 14(12), 2885. <https://doi.org/10.3390/rs14122885>

691 Zulkarnain, I. (2016). Sumatra is not a homogeneous segment of Gondwana derived continel
692 blocks: A New Sight based on Geochemical Signatures of Pasaman Volcanic in West
693 Sumatera. *Jurnal Riset Geologi Dan Pertambangan*, 26(1), 1.
694 <https://doi.org/10.14203/risetgeotam2016.v26.271>

695

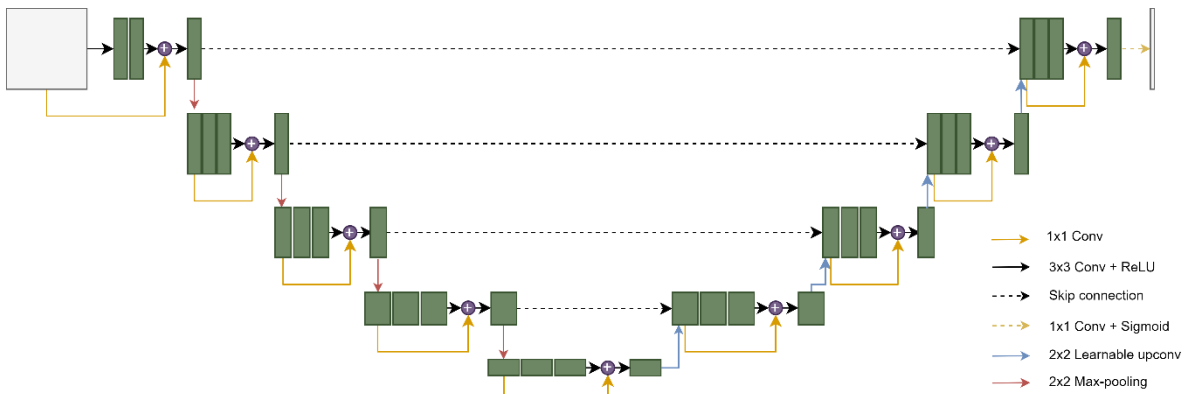
696

697 SUPPLEMENTARY MATERIALS



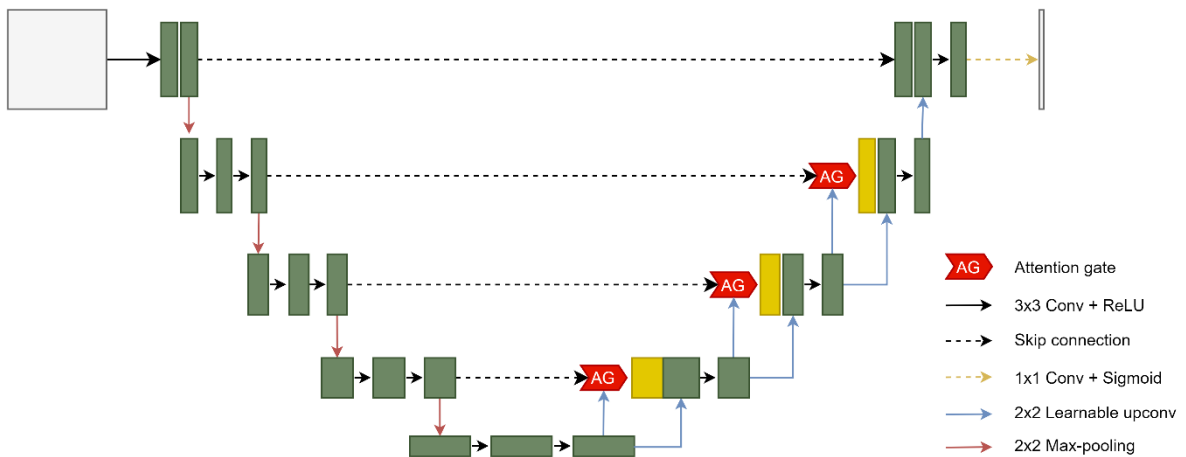
698
699
700
701

Figure S1: Model architecture of the conventional U-Net.



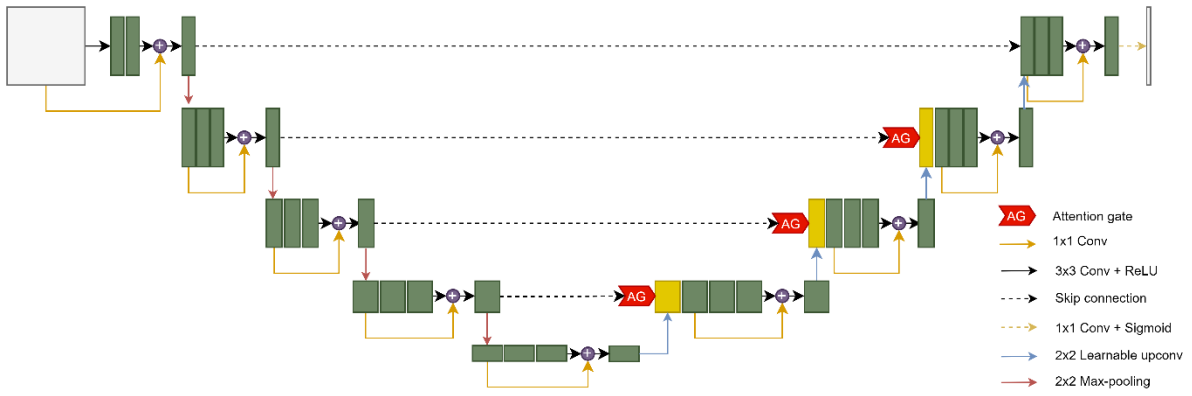
702
703
704

Figure S2: Model architecture of the Res U-Net.

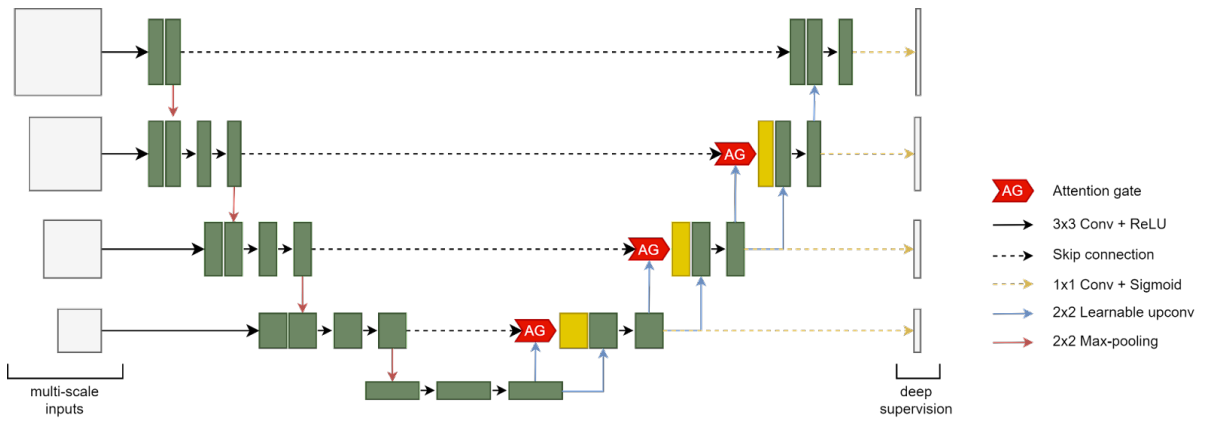


705
706
707
708

Figure S3: Model architecture of the Attention U-Net.



709
710 Figure S4: Model architecture of the Attention Res U-Net.
711



712
713 Figure S5: Model architecture of the Attention Deep Supervision Multi-Scale U-Net.
714
715

716

717

718

719

720